Variability of the ocean-induced magnetic field predicted at sea surface and at satellite altitudes

Roman E. Glazman

Jet Propulsion Laboratory, Pasadena, California, USA

Yury N. Golubev

Raytheon ITSS, Pasadena, California, USA

[1] Spatial and temporal variability of the magnetic field component induced by ocean circulation is investigated on the basis of a standard thin-shell approximation of electro- and magneto-static equations. Well-known difficulties of numerical solution of the governing equations are resolved by reducing the problem to an equation for the electric field potential, Φ, as opposed to a more conventional approach focused on the vertical jump, ψ, of the magnetic field potential across a combined ocean/marine-sediment-layer spherical shell. The present formulation permits using more realistic input data on ocean currents and ultimately yields much greater (by at least an order of magnitude) values of the magnetic field at sea surface than predicted in earlier studies. Such large values are comparable to, and in some cases exceed, magnetic field variations caused by lithospheric and ionospheric sources on monthly to interannual timescales. At the 400-km altitude (of CHAMP satellite), the field attains 6 nT. The model predictions show favorable comparisons with some in situ measurements as well as with Challenging Minisatellite Payload (CHAMP) satellite magnetometer data.

Citation: Glazman, R. E., and Y. N. Golubev (2005), Variability of the ocean-induced magnetic field predicted at sea surface and at satellite altitudes, *J. Geophys. Res.*, *110*, C12011, doi:10.1029/2005JC002926.

1. Introduction

[2] Electro-magnetic induction due to the flow of conducting seawater in the Earth's magnetic field has been a subject of research interest for many years [e.g., *Sanford*, 1971; *Larsen*, 1992; *Stephenson and Bryan*, 1992; *Chave and Luther*, 1990; *Lilley et al.*, 1993, 2001; *Tyler et al.*, 1997; *Flosadottir et al.*, 1997a, 1997b]. Recent increase of research activities [e.g., *Tyler et al.*, 2003; *Vivier et al.*, 2004; *Maus and Kuvshinov*, 2004] is motivated by possible use of spaceborne magnetometers for monitoring ocean currents and tides. An important question to be answered by such studies is whether the magnitude of the ocean-induced magnetic field, **b**, is sufficient for detection by present magnetometers.

[3] In situ measurements at and below the ocean surface demonstrated that this magnitude reaches many tens of nanotesla (nT) [*Lilley et al.*, 2001]. Ocean eddies near Tasmania induce up to 25-nT magnetic fields [*Lilley et al.*, 1993] at the sea surface. However, present numerical models predict much lower values. For example, *Stephenson and Bryan* [1992] found the vertical component, b_z, of the field at the sea surface to be of order 1 nT, while *Tyler et al.* [1997] and *Vivier et al.* [2004] reported field magnitudes within a few nT. One of the goals of the present study is to demonstrate that an accurate numerical implementation of the commonly accepted theory produces values at least an order of magnitude greater. At the CHAMP satellite altitude, our computations produce up to 6 nT, also considerably greater than predicted earlier. The standard deviation of this signal from its long-term time average is within 1 nT, and this is confirmed by our preliminary analysis of the CHAMP data, section 6.

[4] The now standard approach to calculating the ocean-induced signal is due to *Larsen* [1992] and *Stephenson and Bryan* [1992], who employed the thin-shell approximation of the electro- and magneto-static equations and reduced the problem to a single equation for field variations in the horizontal plane **x**:

$$\nabla \cdot \left(K_{eff} \nabla \psi \right) = G(\mathbf{x}). \qquad (1)$$

Here ψ is the vertical jump in the magnetic field potential across the spherical shell comprised of two conducting layers: the ocean and the underlying marine sediment. This function is linearly proportional to the stream function for (the horizontal component of) a vertically integrated electric current [*Larsen*, 1992; *Stephenson and Bryan*, 1992]. $K_{eff}(\mathbf{x})$ is the effective magnetic diffusivity representing the combined sediment and ocean layers: $K_{eff} = [\mu(\Sigma_{oc} + \Sigma_s)]^{-1}$, and $G = -\nabla \cdot [(\Sigma_{oc} + \Sigma_s)^{-1} F_z \mathbf{S}]$ is the ocean-induced "forcing function." Here μ is the

magnetic permeability, and the other parameters are given by equation (11).

[5] As is known from standard literature [e.g., *Richtmyer and Morton*, 1967], and highlighted for the case of ocean-induced fields by *Stephenson and Bryan* [1992], a fully convergent numerical solution of equation (1) is difficult to achieve for large values of K_{eff} and small mesh size. We demonstrate in section 4 that an incomplete convergence may lead to strongly underestimated magnitude of field **b**. This difficulty is resolved in section 2 by reformulating the problem in terms of the electric potential, Φ, which ultimately yields all the other unknowns in a straightforward way. Being equivalent to the more traditional formulation (1), the electric potential equation has great numerical advantages. A fully convergent solution is easily achieved for realistic oceanographic input fields even without a strong preliminary smoothing of these fields (which is necessary when solving equation (1)). This advantage becomes particularly important owing to the fact that modern, eddy-resolving numerical models of ocean circulation, serving as a source of input data for magnetic field calculations, yield much finer spatial structure of oceanographic fields and much greater magnitudes of ocean current velocities than did the ocean models employed in the previous studies.

[6] The main obstacle to inferring the ocean-induced signal either from spaceborne or near-surface in situ magnetometer measurements is the ambient "noise" due to variations of the electric currents in the ionosphere, magnetosphere ("space weather") fluctuations, lithospheric and Earth's main magnetic field variations, etc. Their spatial and temporal scales overlap with energy-containing scales of oceanic variability. Therefore any feasibility study on ocean magnetometry should start with quantitative characterization of the natural variability of the ocean-induced magnetic field. This characterization, based on a rapidly convergent numerical solution for the electric field potential, is produced in section 5. Three-dimensional time-varying fields of oceanographic parameters hindcasted by a high-resolution global ocean numerical ECCO-MIT model [*Fukumori et al.*, 1999; *Lee et al.*, 2002] are used as the input. In its 1°-resolution version, this ocean model assimilates observational data to achieve greater fidelity. As a source of even more realistic input data on oceanic variability, we also use data products from a (1/6)°-resolution version of the ECCO-MIT model. Tidal motions are not included in this analysis.

2. Formulation of the Problem

[7] In this section we summarize an alternative formulation aimed at replacing equation (1) with a computationally more advantageous equation. Both formulations are based on the thin-shell approximation of the Maxwell equations; hence they are fully equivalent in terms of the underlying physics.

2.1. Ocean: $-H < z < 0$

[8] Since we are interested in the effects of large-scale quasi-geostrophic (i.e., slow) motions, the electro- and magneto-static equations for a moving medium in a thin spherical two-layer shell reduce to the following

well-known system for the horizontal components, $\mathbf{E}_\perp$ and $\mathbf{b}_\perp$, of the ocean-induced electric and magnetic fields $\mathbf{E}$ and $\mathbf{b}$,

$$\frac{\partial E_\varphi}{\partial z} = 0 \quad \frac{\partial E_\theta}{\partial z} = 0, \tag{2}$$

$$\frac{\partial}{\partial \theta}\left(E_\varphi \sin \theta\right) - \frac{\partial E_\theta}{\partial \varphi} = 0, \tag{3}$$

$$k_{oc}\frac{\partial b_\theta}{\partial z} + v F_z = -E_\varphi, \tag{4}$$

$$k_{oc}\frac{\partial b_\varphi}{\partial z} + u F_z = E_\theta, \tag{5}$$

where the subscripts φ and θ label the zonal and meridional components, respectively. (By the vertical components (such as F_z) and vertical derivative (∂/∂_z) we imply radial components and radial derivative (∂/∂_r).) The meridional coordinate, θ, represents the co-latitude (changing from 0 to π starting at the North Pole). The full magnetic field $\mathbf{B} = \mathbf{F} + \mathbf{b}$ contains a much larger, 3D component due to the Earth's main field $\mathbf{F}$, of which only the radial component F_z is important at middle to high latitudes. The spatial distribution of this component has been derived based on the CHAMP CO2 model [*Holme et al.*, 2003] as a 3-year mean for the period 2001–2003. The magnetic diffusivity coefficient $k_{oc} = (\mu\sigma_{oc})^{-1}$ is a function of all three coordinates, although the horizontal scale of its variations is very large by comparison to the vertical scale. This coefficient is controlled by the electric conductivity σ_{oc} of seawater whose local, time-varying values are computed based on water temperature and salinity. These quantities, as well as the time-varying field of the horizontal velocity $\mathbf{u} = (u, v)$, are obtained at 46 depth levels from the 1° ECCO-MIT numerical model used at JPL [*Fukumori et al.*, 1999] and at 50 levels for the (1/6)° version of this model.

2.2. Marine Sediment: $-(H + h) < z < -H$

[9] As in most of the preceding studies, we account for the electric current in the sediment layer, but assume the underlying rock mantle to be nonconductive. Therefore equations (2)–(3) remain unchanged at $-(H + h) < z < -H$, while equations (4) and (5) become

$$k_s\frac{\partial b_\theta}{\partial z} = -E_\varphi, \quad k_s\frac{\partial b_\varphi}{\partial z} = E_\theta. \tag{6}$$

The relatively small conductivity σ_s of marine sediments makes k_s an order of magnitude greater than k_{oc} [e.g., *Sanford*, 1971; *Larsen*, 1992].

[10] An alternative approach accounting for the conductivity of the rock mantle is presented by *Kuvshinov and Olsen* [2004]. However, for the case of tidal motions, they find only a small decrease (within 20% in the scalar magnitude of magnetic field) by comparison to the *Tyler et al.* [2003] model which treats the Earth mantle as an

insulator. In the absence of direct measurements of the mantle conductivity, either approach leaves wide room for speculations about the actual properties of the Earth mantle and their relevance to the problem at hand. While adhering to a more common view that discards the mantle currents as being negligible by comparison to the electric currents in the ocean and sediment layers, we delegate it to future observational studies to rate the validity of either approach.

2.3. Boundary Conditions

[11] Assuming the absence of electric current j_z across the top and bottom boundaries of our spherical shell, we impose, based on the Ampere law $\mathbf{j} = \mu \cdot \nabla \times \mathbf{B}$, the following (zero curl) condition at $z = 0$ and $z = -(H + h)$:

$$\frac{\partial}{\partial \theta}(b_\varphi \sin\theta) - \frac{\partial b_\theta}{\partial \varphi} = 0. \qquad (7)$$

This will soon be used to reduce equations (2) (3) (4)–(5) to a single equation for the electric field potential from which all other unknowns follow immediately.

[12] Remaining boundary conditions are standard: We demand the continuity of $\mathbf{b}_\perp$ and $\mathbf{E}_\perp$ across the ocean floor ($z = -H$) and constrain the vertical jump $\delta_z\mathbf{b}_\perp = \mathbf{b}_\perp(z = 0) - \mathbf{b}_\perp(z = -H - h)$ of the horizontal component across the spherical shell using a well-known relation [e.g., *Stephenson and Bryan*, 1992] between the field's vertical components at the top and bottom boundaries of the two-layer shell: $b_z(z = 0) = b_z(z = -H - h)$. In terms of the magnetic field potential χ (defined at $z \geq 0$ and $z \leq -H - h$), this is

$$\left.\frac{\partial\chi}{\partial z}\right|_{z=0} = \left.\frac{\partial\chi}{\partial z}\right|_{z=-H-h}. \qquad (8)$$

As shown in Appendix A, if ocean-induced variations occur only on short (compared to the Earth radius) spatial scales, condition (8) leads to a very convenient approximation relating the field's horizontal components on both sides of the shell,

$$\mathbf{b}_\perp(z = 0) \approx -\mathbf{b}_\perp(z = -H - h). \qquad (9)$$

This approximation will be used in section 4 for crude estimates based on in situ measurements of oceanographic parameters.

[13] For our purpose, the values of $\mathbf{b}_\perp$ are needed only at the sea surface. Equations (4)–(6) yield

$$\delta_z\mathbf{b}_\perp = \mu\Sigma_{oc}(1 + \lambda)\mathbf{E}_\perp \times \mathbf{n} - \mu F_z\mathbf{S}, \qquad (10)$$

where $\mathbf{n}$ is a radial unit vector. In a component form this is $\delta_z b_{\varphi,\theta} = (\pm)\mu\Sigma_{oc}(1 + \lambda)E_{\theta,\varphi} - \mu F_z S_{\varphi,\theta}$, where the sign of the first term in the r.h.s. depends on a subscript selected in the l.h.s. The surface field is thus the sum of an electric field term determined by the "global" solution of equation (12) and a local induction term. The other notations are

$$\Sigma_s = \int_{-H-h}^{-H}\sigma_s dz, \quad \Sigma_{oc} = \int_{-H}^{0}\sigma_{oc}dz, \quad \mathbf{S} = \int_{-H}^{0}\mathbf{u}\sigma_{oc}dz, \quad (11)$$

where $\mathbf{S}$ is the electric conductivity flux, and $\lambda = \Sigma_s/\Sigma_{oc}$ characterizes the electric current leakage from the ocean to the sediment layer. Its characteristic value is known to be small: λ 0.1 [*Lilley et al.*, 1993], and its exact value has little effect on the end result. In general, λ, Σ_{oc}, H, h, and $\mathbf{S}$ are slow functions of φ and θ.

2.4. Electric Field

[14] Taking the curl of equation (10) and using equation (7) yields a 2D Poisson-type equation for the electric field potential in the ocean+sediment (spherical) shell,

$$\nabla_\perp \cdot [\Sigma_{oc}(1 + \lambda)\nabla_\perp\Phi(\varphi, \theta)] = \nabla_\perp \times (F_z\mathbf{S}), \qquad (12)$$

where

$$E_\varphi = -\frac{1}{a\sin\theta}\frac{\partial\Phi}{\partial\varphi}, \quad E_\theta = -\frac{1}{a}\frac{\partial\Phi}{\partial\theta}. \qquad (13)$$

It is easy to show that equation (12) also follows from the electric charge conservation law, $\nabla \cdot \mathbf{j} = 0$, integrated over z under the boundary condition $j_z = 0$ at the upper and lower boundaries, combined with a thin-shell version of Ohm's law. The full, 3D version of equation (12) was used by *Flosadottir et al.* [1997a, 1997b] to model the ocean-induced electric field in the North Atlantic. We shall solve equation (12) for the entire globe. Within the continents, the flow velocities (hence, the r.h.s. of equation (12) becomes zero, and we additionally assume that the inland conductivity field is spatially homogeneous. This global formulation permits the use of spatially periodic boundary conditions for both the field potential and its gradient around the globe. As a result, an unambiguous solution of equation (12) becomes possible. Apparently, this solution will contain errors in coastal regions due to the simplification of the continental electric field. However, such errors have little effect on the solution in the open ocean. With $\mathbf{E}_\perp$ obtained from equations (12)–(13), the magnetic field at the surface follows from equations (10) and (8) as explained in the end of this section. Once $\mathbf{b}_\perp(\varphi, \theta, z = 0)$ is found, the magnetic field at any ocean depth follows from equations (4) and (5).

2.5. Magnetic Field at and Above the Ocean Surface

[15] The atmospheric problem reduces to the Laplace equation for the magnetic field potential, $\Delta\chi = 0$, (where $\Delta \equiv \nabla \cdot \nabla$). With $\delta_z\mathbf{b}_\perp(\varphi, \theta)$ given by equation (10), the surface potential, $\chi_0(\varphi, \theta)$, can be computed using the boundary condition (8) as described in Appendix A. However, prior to this step, we have to determine the "electric current stream function," $\psi = \chi(\varphi, \theta, z = 0) - \chi(\varphi, \theta, z = -H - h)$, by solving equation

$$\nabla_\perp\psi = \delta_z\mathbf{b}_\perp. \qquad (14)$$

The formal solution, given by the line integral $\psi(\varphi, \theta)$

$$\psi = \oint_L \delta_z\mathbf{b}_\perp^0(\varphi', \theta') \cdot d\boldsymbol{\xi}'_\perp + C, \qquad (15)$$

is known only up to a constant C. Here L is an arbitrary curve on the ocean surface connecting an arbitrary point

(φ_0, θ_0) with the current point (φ, θ). The integration constant represents the value of ψ at point (φ_0, θ_0). As a test of goodness of the numerical solution for $\delta_z \mathbf{b}_\perp$, we verify that it satisfies the no-curl condition stemming from equation (7) which guarantees that the line integral (15) is indeed independent of the path L.

[16] The resulting $\psi(\varphi, \theta)$ ultimately (as shown in Appendix A) permits an unambiguous determination of the horizontal field $\mathbf{b}_\perp(z = 0) = \nabla_\perp \chi$, but not of the vertical component b_z. To obtain the latter, one has to determine the integration constant in equation (15). This can be done using either of the following two approaches. Let us assume that inside a continent, far enough from the coastline, the ocean-induced field ψ attenuates to zero. Placing the initial point (φ_0, θ_0) of the integration path L in such an inland area, we can set $C = 0$ and thus determine the magnetic potential at any point of the ocean surface unambiguously. An alternative approach (ultimately yielding the same result for $\chi(\varphi, \theta)$) is to demand the spatially periodic boundary condition for the field ψ (as well as for its horizontal gradient) around the globe, in the fashion of a similar procedure used earlier with equation (12). Such conditions are applied to the Poisson equation $\Delta_\perp \psi = \nabla_\perp \cdot \delta_z \mathbf{b}_\perp$ obtained by taking the gradient of equation (14).

[17] Given $\chi(z = 0)$, the magnetic potential in the half-space above the ocean can be obtained using a Green formula,

$$\chi(\mathbf{x}) = 14\pi \int_A \frac{\partial G(x, \boldsymbol{\xi})}{\partial n} \chi_0(\varphi', \theta') d\boldsymbol{\xi}' \qquad (16)$$

where $G(\mathbf{x}, \boldsymbol{\xi})$ is the Green function of the Dirichlet problem for the Laplace equation with a spherical boundary A [e.g., *Jackson*, 2002]. In this equation, the vertical distance x_3 is measured from the center of the Earth, i.e., $x_3 \equiv r$. In practice, a computationally more efficient approach to solving both equations (14) and (16) is based on the spherical harmonic expansion, Appendix A.

3. Estimates Based on in Situ Oceanographic Measurements

[18] The accuracy of the modeling results in section 5 depends on the accuracy of the numerical solution of the governing equations of section 2 and on the accuracy of oceanographic fields supplied by the ECCO-MIT model. These two issues are briefly discussed in this section.

3.1. Validation of ECCO-MIT Model Data Products

[19] We compared ocean current velocities hindcasted by the $1°$ and $(1/6)°$ versions of the ECCO-MIT model with several field observations by ocean current moorings and found that the $1°$ model tends to systematically underestimate the velocities, whereas the $(1/6)°$ version yields much more satisfactory results in terms of the characteristic amplitudes of the vertically integrated horizontal velocities. Figure 1 illustrates time histories of observed and predicted velocities at 51.03°S, 143.24°E where our model predicts particularly high values of the magnetic field. At this site, the relative r.m.s. error between the observed and modeled amplitudes of the monthly averaged horizontal transport was about 10% for the $(1/6)°$ ECCO-MIT model but over

80% for the $1°$ model. This trend was confirmed for a few other locations randomly selected for our comparisons. A more systematic analysis of the ocean model performance would require a special study that would take us well outside the scope of the present work.

[20] Additionally, we compared the values of electric conductance Σ_{oc} computed from vertical profiles of water temperature and salinity derived from model hindcasts with the conductance based on the profiles of the monthly mean temperature and salinity from the Levitus climatology. In terms of their effect on the predicted values of the magnetic field, the differences were negligible. As further discussed in section 5, long-term averages of the ocean conductance can be used in place of the actual instantaneous values with little loss of accuracy.

3.2. Estimates of Magnetic Field Based on in Situ Measurements

[21] As known from the previous studies, see also our section 5, the two terms in the r.h.s. of equation (10) are of comparable magnitude, although the second term is typically about twice as large as the first one. This fact, together with equation (9), allows one to estimate the characteristic magnitude of the horizontal field at the sea surface as

$$b_\perp(z = 0) \approx \mu F_z S. \qquad (17)$$

In order to compute $\sigma_{oc}(z)$ and S we used vertical profiles of ocean current velocities observed at two locations and climatological data on ocean temperature and salinity. The experimental sites and the results are listed in Table 1. Two profiles shown in Figure 2 represent hourly measurements averaged over the periods of observations reported in Table 1. Site A was selected because its local depth and characteristic current velocities are not too different from those relevant to the field experiment of *Lilley et al.* [1993]. Region B was selected owing to particularly high values of both F_z and S at this location. The local values of F_z are from *Holme et al.* [2003]. For region A, the value of $b_\perp$ is in good agreement with the measurements by *Lilley et al.* [1993] under comparable oceanographic conditions. As shown in section 5, this $b_\perp$ also agrees with our numerical model predictions based on the $(1/6)°$ resolution ECCO-MIT model.

4. Numerical Experiments

[22] Although both equations (1) and (12) are of the same (elliptic) type, their numerical properties are dramatically different due to a large difference in the magnitude of the (properly scaled) coefficients entering their l.h.s. Efficient numerical techniques for elliptic equations employ relaxation schemes [e.g., *Fletcher*, 1988] wherein the relaxation parameter α is selected (empirically) to yield a fully convergent solution after a minimal number of relaxation steps ("iterations"). In general, the convergence rate is higher for greater values of α. However, α must be kept below a certain critical value in order to prevent a numerical solution from "blowing up." *Stephenson and Bryan* [1992] discuss this issue with respect to equation (1).

[23] We carried out numerical experiments for both equations (1) and (12) using the same (global) input fields
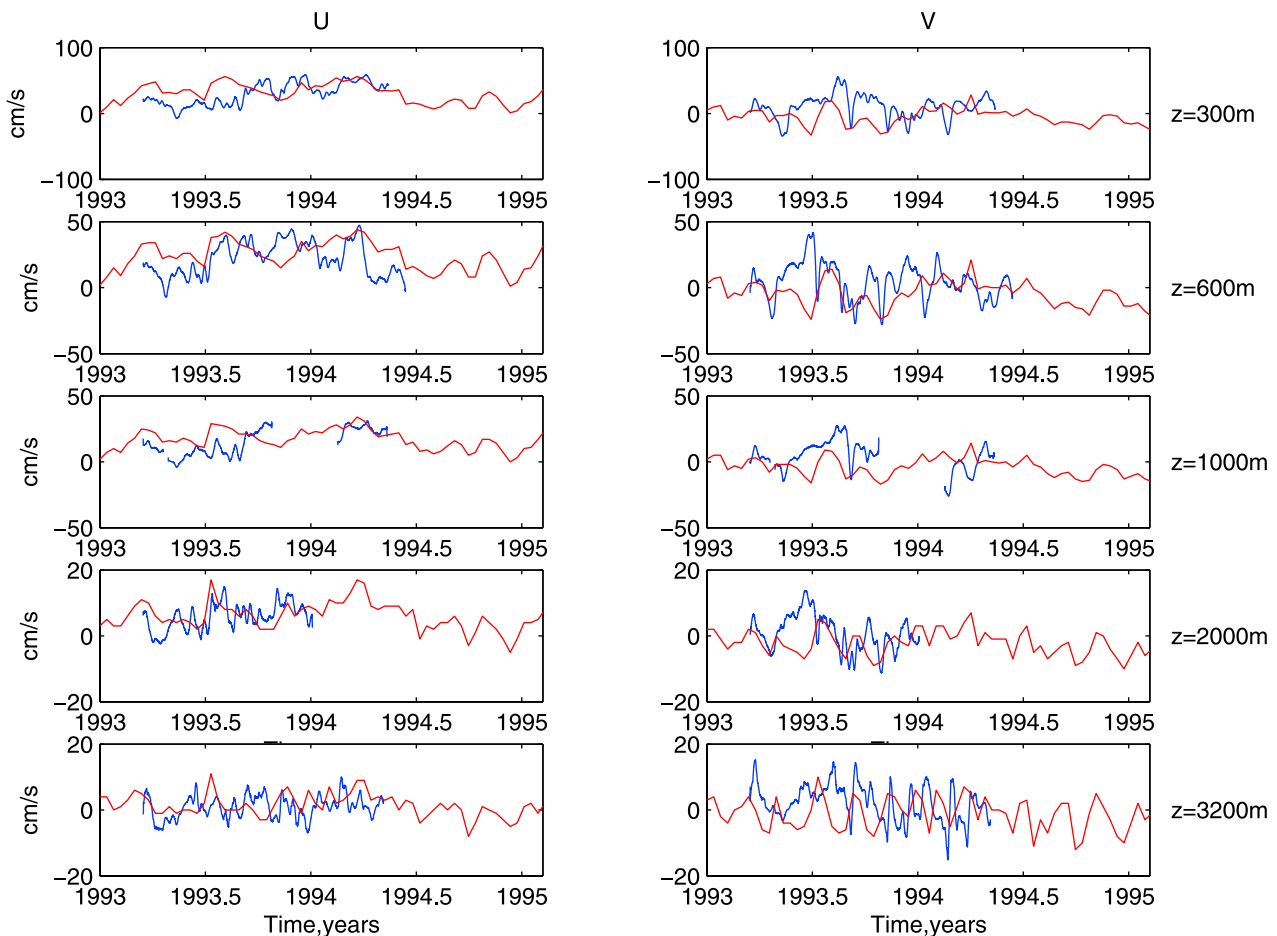
Figure 1. Comparison of ocean current velocities predicted by the $(1/6)°$ version of the ECCO-MIT model with observations at a buoy mooring located at 51.03°S, 143.24°E. Red curves, model prediction; blue curves, ocean current meter data.

from the 1° version of the ECCO-MIT model. Table 2 illustrates the results for equation (1) for which we had to smooth the input fields twice in order to achieve convergence. In Case 1 the iterations were stopped when the relative error, ϵ, (between two steps) dropped down to 10%. This required 88 iterations with $\alpha = 0.15$ but only half that number with $\alpha = 0.3$. Setting more rigid requirements on ϵ, we discovered that the "10% solution" was far from fully convergent, as illustrated in columns 4 and 5 of Table 2. The full convergence was achieved only by using an extremely rigid criterion (Case 4: $\epsilon \leq 0.01\%$), which required over 10^4 iterations. Further reduction of ϵ did not appreciably affect the end results. With $\alpha > 0.31$, the solution would not converge at all.

[24] The fully convergent solution for equation (12) was possible even without preliminary smoothing of the input fields. The full convergence was achieved with $\alpha = 1.5$ after less than 10^2 iterations. This solution (in terms of b_z)

was then compared with the fully convergent solution of equation (1) showing rather insignificant differences. The use of ocean data products from a $(1/6)°$ version of the ECCO-MIT model caused even more severe difficulties for equation (1), requiring a strong (triple) preliminary smoothing of the input data and taking well over 10^5 iterations.

[25] We thus conclude that using a "reasonable" criterion of convergence (such as $\varepsilon = 5\%$ employed by *Stephenson and Bryan* [1992]) does not guarantee full convergence for equation (1) and tends to yield much smaller values of the magnetic field than are obtained at full convergence. On the contrary, equation (12) permits using "over-relaxation" techniques with α as high as 1.5, and the fully convergent solution is achieved after only about 10^2 iterations.

[26] To ensure the correctness of the field potential χ at the sea surface and above, we compared the following independent approaches to solving the problems stated by

Table 1. Magnetic Field Estimates Based on Ocean Current Measurements

Station	Latitude, °S	Longitude, °E	Depth, m	Starting Date	Duration, months	S, m/s/ohm	F_z, nT	$b_\perp$, nT
A	31.17	30.54	2498	3 March 1995	1.5	831	2.5×10^4	26.1
B	51.03	143.24	3800	3 December 1993	14	2004	6×10^4	151. 3
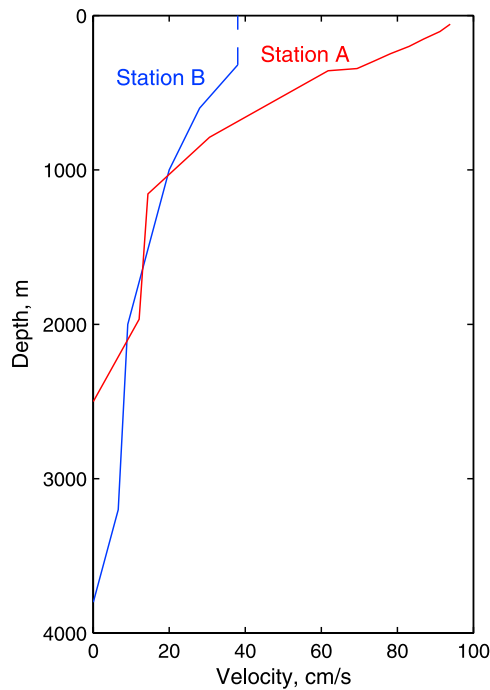
Figure 2. Vertical profiles of horizontal velocity amplitudes averaged over the periods of observations shown in Table 1, for two locations in the Indian Ocean.

equations (14), (8), and (16). Specifically, the closed-form solution (15) of equation (14) was compared to a numerical solution of the Poisson equation $\Delta_\perp \psi = \nabla_\perp \cdot \delta_z \mathbf{b}_\perp$ showing little difference. These solutions were then expanded in spherical harmonics to apply the boundary condition (8) as explained in Appendix A. The Spherepack package (J. C. Adams and P. N. Swarztrauber, SPHEREPACK 3.1: A Model Development Facility, available at www.scd.ucar.edu/css/software/spherepack/index.html) greatly facilitated these computations. The resulting surface potential was used as χ_0 in equation (16) to compute the field above the ocean. These results were then compared with the "spherical harmonics" solution obtained by expanding the r.h.s. of equation (14) and computing the corresponding coefficients δ_{nm} of equation (A4). The magnetic field potential at and above the surface was then determined using equations (A6) and (A1). At the altitudes above 50 km, this solution was almost identical to the result based on the Poisson equation for ψ and the Green function expression for χ. At lower altitudes, the use of equation (16) is impractical. The spherical harmonics approach is computationally least expensive and it was ultimately used to

obtain all the results described in section 5. However, the intercomparison of all three approaches confirmed the validity and sufficiently high accuracy of the results reported in section 5.

5. Analysis of Magnetic Field Variability

[27] Using temperature, salinity and horizontal velocities hindcast at all depth levels by the global ocean numerical ECCO-MIT model we computed the ocean-related parameters Σ_{oc} and $\mathbf{S}$ for subsequent use in the electric and magnetic field computations described in section 2. Equation (12) was then solved for each time instant using the successive over-relaxation method [Fletcher, 1988] with the relaxation parameter $\alpha = 1.5$ for the $1°$ version and $\alpha = 0.9$ for the $(1/6)°$ version of the ECCO-MIT model. The results presented in Figure 3 and in Figure 8 (later in this section) are based on the $(1/6)°$ version of the ECCO-MIT model, while the results in Figures 4–7 were obtained using the $1°$ version and computing all fields every 10 days for the 11 year period of simulations starting in January 1993. As explained in section 3, the $(1/6)°$ ECCO-MIT model yields ocean currents in a much better agreement with observations than does the $1°$ version. However, as we found through numerical experiments, the corresponding differences in the magnetic field at the satellite altitude are rather small (about 20%). This happens because the $1°$ model, while missing short-scale horizontal variability (containing a significant fraction of the kinetic energy), reproduces large-scale features of ocean dynamics reasonably well. The short-scale variations of the magnetic field attenuate with height much faster than do variations caused by the large-scale oceanic variability. Being rather adequately reproduced by the coarser $1°$ model, this variability also dominates the fields at high altitudes (as illustrated by Figure 8). Because of the high computational cost of using the $(1/6)°$ ocean model, we preferred the $1°$ model for statistical analysis requiring 11 years worth of model simulations illustrated in Figures 4–7.

[28] In order to assess the relative importance of temporal variability of electric conductivity, we averaged this quantity over the entire 11-year period and used the resulting mean field to recompute the magnetic fields for July and January of 1998. The end results showed little difference from the fields presented in Figure 3. Therefore the magnetic field's temporal variations are controlled by the temporal variations of ocean currents. For all practical purposes, the instantaneous field $\sigma_{oc}(\varphi, \theta, z, t)$ can be replaced with its "climatological" mean $\sigma_{oc}(\varphi, \theta, z)$. Finally, we estimated relative contributions of the electric field and direct ocean induction terms in equation (10) to

Table 2. Analysis of Numerical Solution of Equation (1)[a]

Case Number	ϵ, %	Number of Iterations		Mean $|\chi|$, m × nT		Max $|b_z|$, nT	
		$\alpha = 0.15$	$\alpha = 0.3$	$\alpha = 0.15$	$\alpha = 0.3$	$\alpha = 0.15$	$\alpha = 0.3$
1	10	88	45	146.8	149.4	4.5	4.5
2	1	701	356	512.5	530.4	11.5	11.5
3	0.1	4042	2021	1104.0	1175.9	12.6	12.6
4	0.01	21,601	10,187	1510.7	1533.4	12.7	12.7

[a]Dependence of the magnitude of the ocean-induced magnetic field on the error convergence parameter ϵ, for two values of the relaxation parameter α. The first in each pair of values in columns 3 through 5 corresponds to $\alpha = 0.15$, and the second pair correspond to $\alpha = 0.3$.
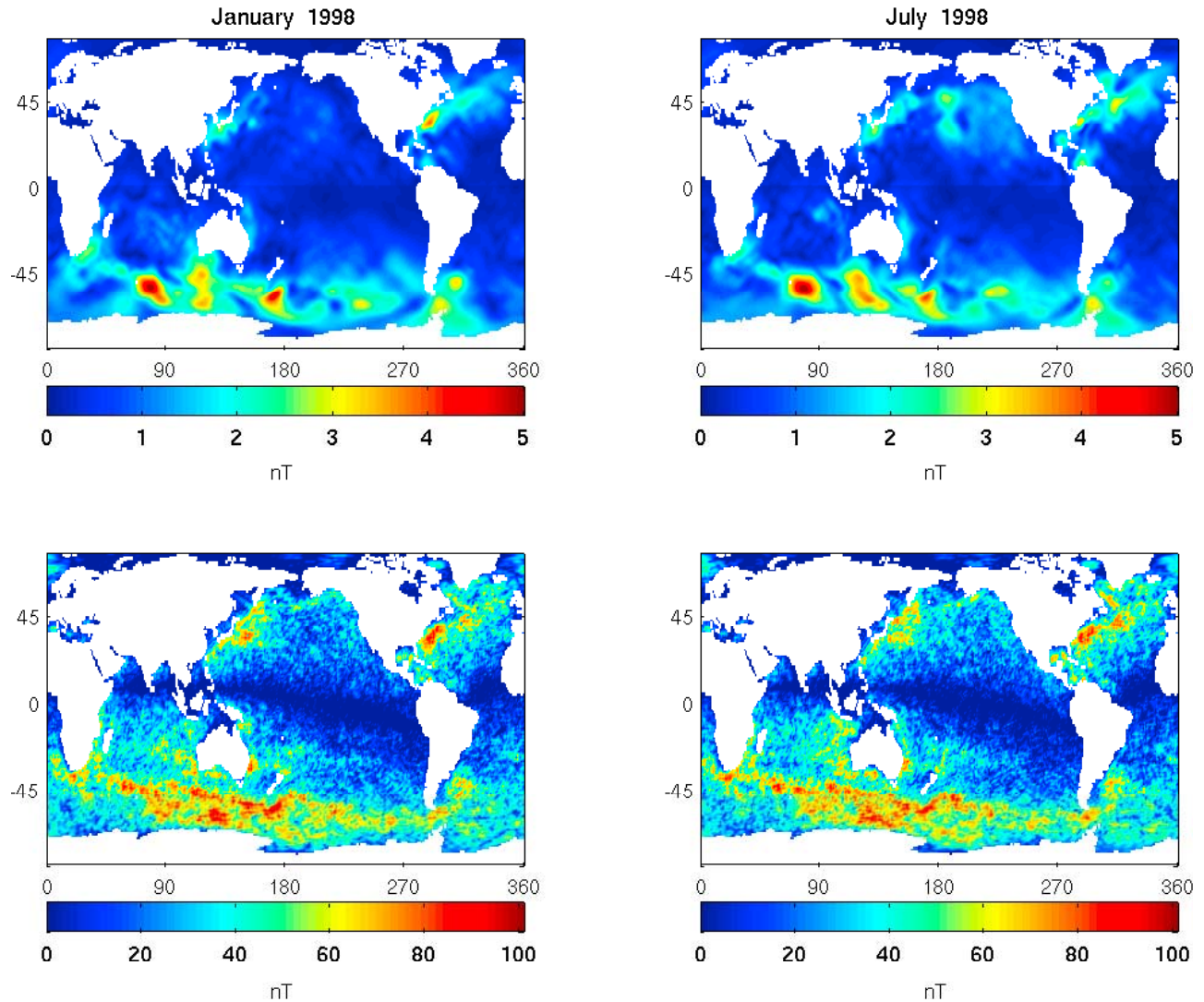
Figure 3. Instantaneous magnetic fields for (left) winter and (right) summer seasons. (bottom) Magnitude, $b = |\mathbf{b}|$, of the field at the sea surface. (top) Magnitude, b, at 430 km above the sea level.

the total ocean-induced magnetic field and found that the second term in the r.h.s. of equation (10) accounts for about 60–70% of the total signal.

[29] As found in the previous studies [e.g., *Stephenson and Bryan*, 1992] (and confirmed by our numerical experiments), specific values of λ have a relatively small effect on the solution of equation (12). In other words, variations of the marine sediment conductivity do not appreciably affect the magnetic field at sea surface. Following earlier recommendations [*Lilley et al.*, 1993], we used λ = 0.1. The solution for the North Atlantic was compared with the solution obtained earlier by *Flosadottir et al.* [1997a, 1997b]. The latter authors accounted for spatial variations of marine sediment and inland conductivity and imposed the vanishing of the electric field potential with an inland distance away from the coastline. Despite such differences, both solutions showed a good mutual agreement both in the magnitude and pattern of electric field variations across most of the Atlantic basin.

[30] In Figure 3 we demonstrate model predictions for the ocean-induced magnetic field at the sea surface and

CHAMP satellite altitude. These results confirm earlier findings [e.g., *Stephenson and Bryan*, 1992] that the largest signal occurs in subregions of the Antarctic Circumpolar Current. However, our surface field is almost 2 orders of magnitude greater than predicted in all previous studies. Appreciable magnitudes are found also in many other regions including the Gulf Stream and Kuroshio systems. At the sea surface, the amplitude of **b** attains 110 nT in several spots south of Australia, while at the satellite altitude its maximum value is 6 nT, also much larger than in the earlier studies. Similar calculations using ocean data products from the 1° version of the ECCO-MIT model yield 20 nT as the maximum amplitude of the surface field, and 4 nT at 430 km.

[31] In the absence of an accurate model of the "external" magnetic field variations caused by non-oceanic factors, manifestations of the ocean-induced signal are difficult to discern from the noisy background. One possible approach is to investigate fluctuations of the observed field about its long-term mean. Magnetic field fluctuations on time-scales corresponding to the characteristic scales of oceanic
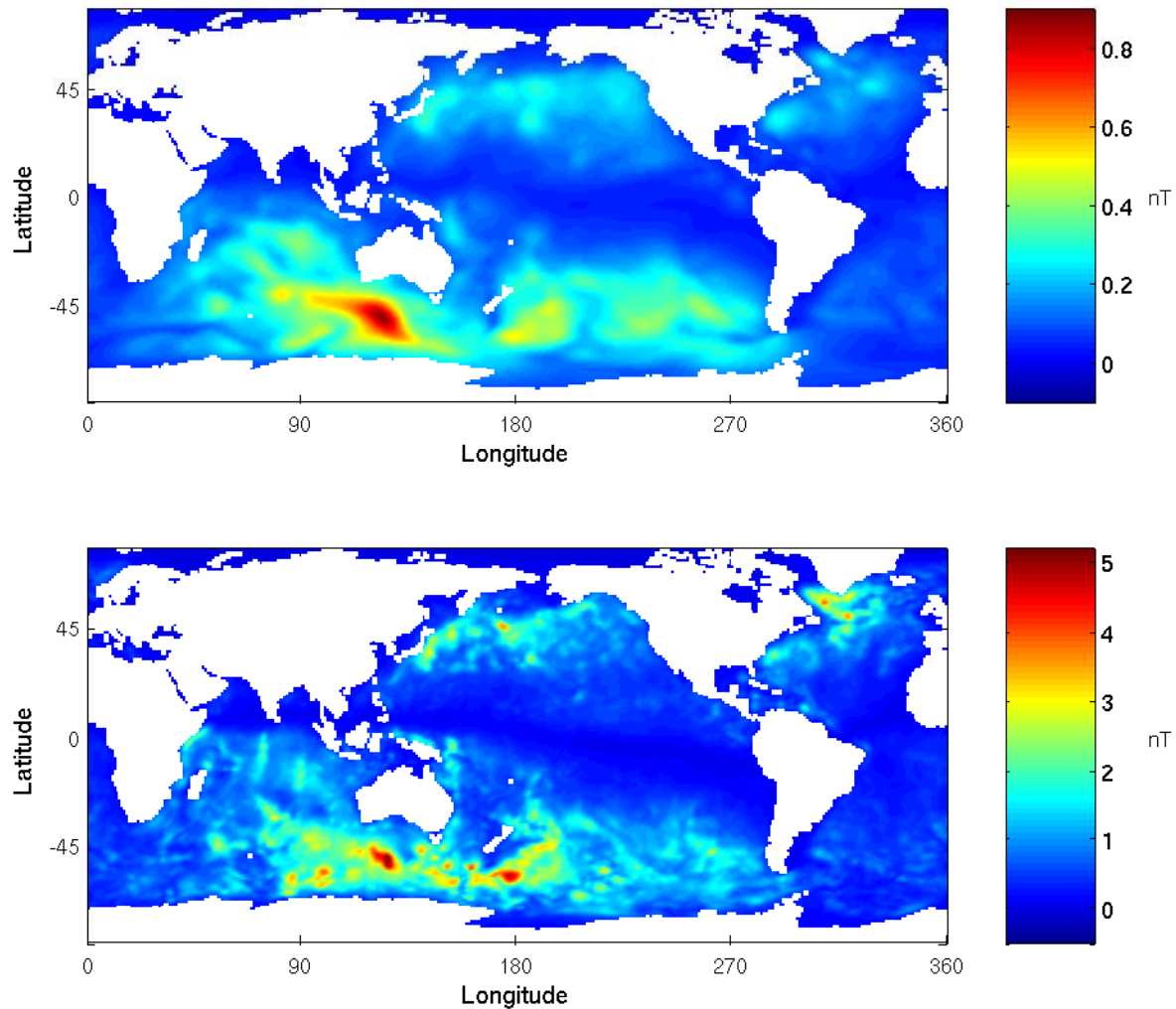
Figure 4. Standard deviation σ_b of the instantaneous magnitude $|\mathbf{b}|$ of the ocean-induced magnetic field from its 11-year mean: (top) 430 km above the sea level and (bottom) at sea level.

variability can be extracted from satellite magnetometer data, as for example done in section 6, and compared with model predictions. Foreseeing such applications, we estimated the size of ocean-induced fluctuations based on the standard deviation of field b from its long-term mean. The pattern predicted in Figure 4 shows two regions of the Southern Ocean as particularly attractive for observational studies. The distribution of this variance over different timescales can be inferred from frequency spectra of magnetic field temporal variations at particular locations.

[32] Such spectra were computed as follows. First, we applied the Lee filtering algorithm [*Lee*, 1986] to the time histories of the magnetic field amplitude and of the ocean transport components, in order to reduce adverse effects of statistical outliers in the time series. Parameters σ (the threshold based on the standard deviation) and N (the size of the record segment) were assigned values 5 and 3, respectively, which led to the suppression of high-frequency noise on scales less than 2 months, but had little effect on the total variance and the spectral shape at frequencies below a 3-month (i.e., seasonal) timescale. For each region

described in Figures 5–7, and for every field under study, we computed four spectra using model data at four neighboring points (about 100 km apart) in a given area. The spectra in Figures 5–7 represent averages over four spatial points, and hence describe temporal variability representative of an individual cell of our computational $1 \times 1°$ grid. As evident from these plots, magnetic field variability at the satellite altitude is dominated by annual timescales, although semi-annual and inter-annual scales can make comparable contributions depending on a region. Not all of the local peaks observed in the spectra of ocean currents are manifested in the magnetic field spectra at the satellite altitude. In other words, the filtering effect of geometric attenuation of the magnetic field with the distance away from the surface is different for oceanic motions of different timescales. In particular, annual and semi-annual oscillations are affected less than oscillations at most other timescales. A rather dramatic example of this effect is illustrated by the spectra of Figure 7. In such regions, inter-annual variability represents the strongest component to be observed both at sea surface and at satellite altitude.
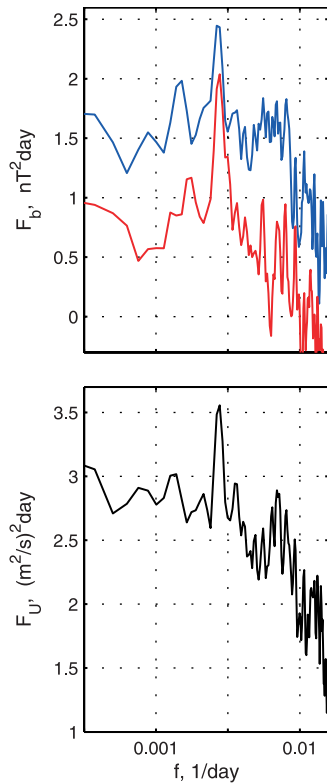
Figure 5. Frequency power spectra of (bottom) the ocean horizontal transport and (top) magnetic field amplitude in an ACC area centered at 122.5°E, 47.5°S. Blue curve, b^{ATM} at sea surface; red curve, b^{ATM} at 430 km altitude. The frequency axis is logarithmic.

[33] The self-explanatory Figure 8 illustrates spatial variability of an instantaneous magnetic field (corresponding to the right panels of Figure 3). At the CHAMP satellite altitude, typical scales of latitudinal variations are about 500 km and these variations are in a few nT range.

6. Preliminary Analysis of CHAMP Satellite Data

[34] Since the ocean-induced signal is small by comparison to other factors of satellite-observed variations of the magnetic field, its extraction requires development of special techniques to remove "external" fields. Empirical models based on the spherical harmonics decomposition of the time-varying fields observed at different altitudes are in a state of rapid development, and may eventually provide necessary help. Such models attempt to describe "external" fields associated with individual factors, such as the main Earth field, the Earth's crustal component, the ionospheric and magnetospheric contributions, etc. However, as our present experience has shown, even the latest CM4 model [*Sabaka et al.*, 2004] does not yet yield a sufficiently "clean" residual. After we have removed crustal, ionospheric and magnetospheric fields (retaining only nightly observations during magnetically quiet periods), the residual still exhibited variations in time as well as along satellite (near-meridional) passes in excess of 10 nT. These variations exhibited neither geographic nor temporal correlations with the ocean signal. Owing to the fact that the time-averaged ocean-induced signal is difficult to
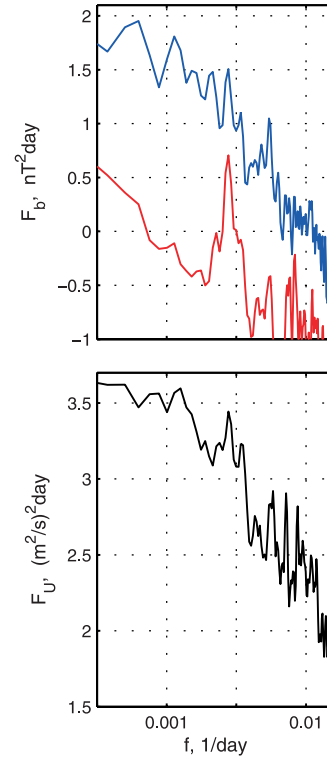
Figure 6. Same as Figure 5, but for a Labrador Sea area centered at 59.5°N, 55.5°W.

separate from the crustal signal when developing an empirical model of the latter, the CM4 model mixes these two fields together (T. Sabaka, personal communication, 2004). Eventually, we concluded that we cannot achieve
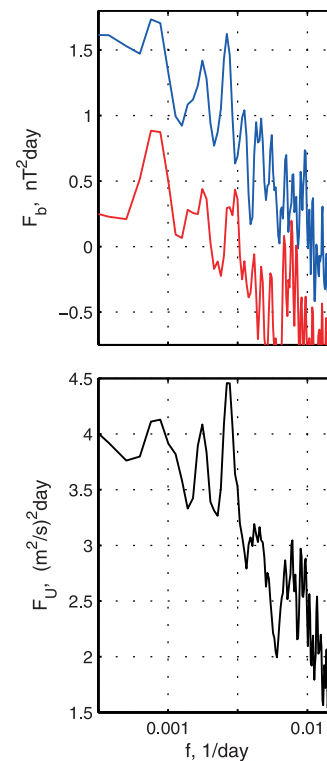
**Figure 7.** Same as Figure 5, but for an ACC area east of New Zealand centered at 40°S, 180°.
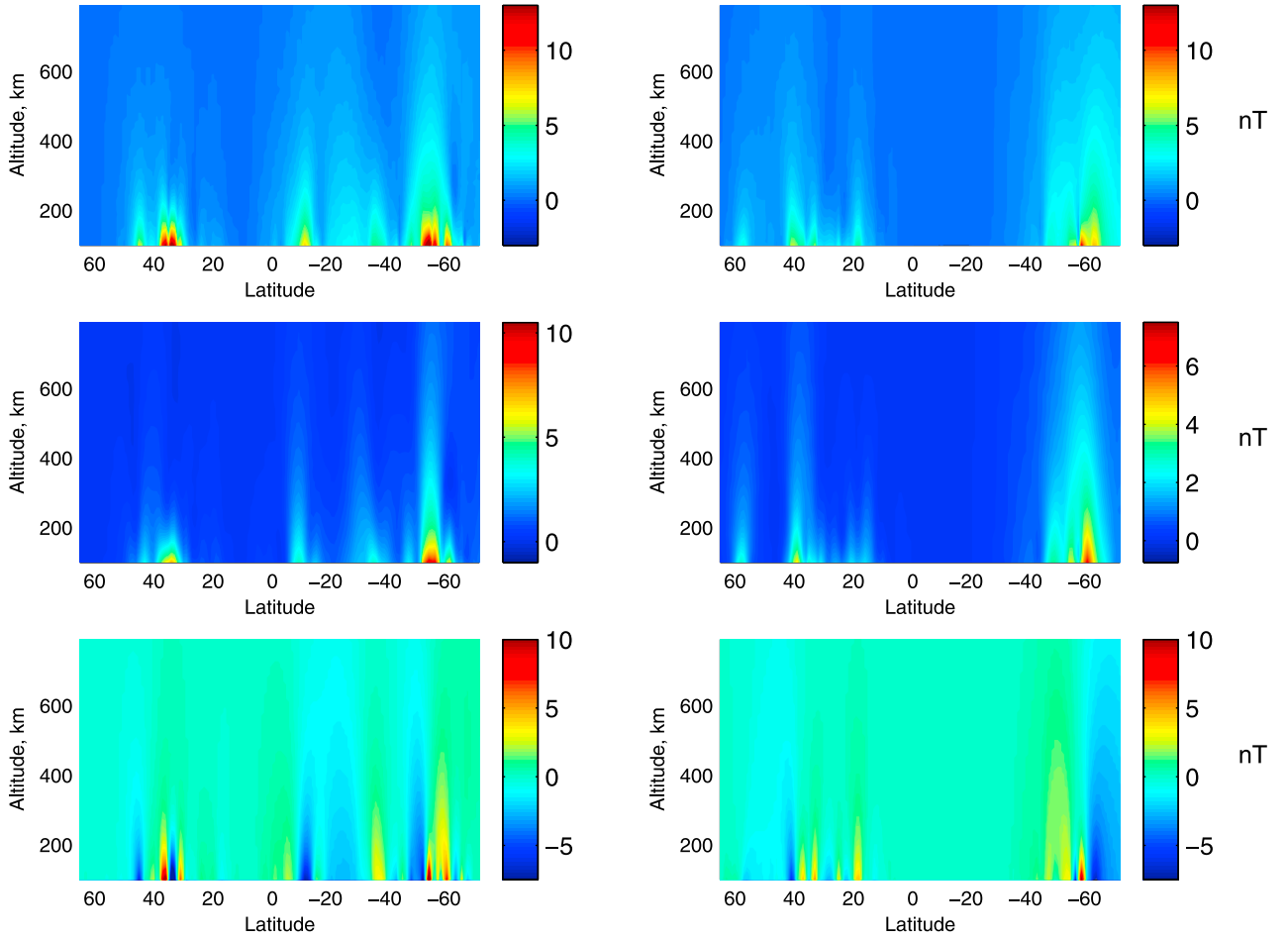
Figure 8. Meridional sections of the ocean-induced magnetic field at (left) 150°E and (right) 60°W, for June 1998. (bottom) Vertical component b_z. (middle) Magnitude, $b_\perp = |\mathbf{b}_\perp|$, of the horizontal component. (top) Full scalar field $b = |\mathbf{b}|$.

the desired accuracy by using present empirical models of individual components of the total field in order to extract the residual due to the ocean-induced signal.

[35] We then shifted our attention to the spatial distribution of the standard deviation of the properly filtered signal from its long-term average. Figures 9 and 10 show the RMS deviation of the CHAMP observed magnetic field from its 2.5-year mean. These results were obtained using the following procedure. The CHAMP data (separately for each orthogonal component of the observed field) were high-pass filtered along satellite passes to retain only spatial variations with scales shorter than 10^3 km. This served to remove the main Earth field, the large-scale components of crustal and magnetospheric signals, and the variations induced by a constantly changing altitude of the satellite. These data were then binned into time-space cells with the dimensions of 1 month, $5°$ in the zonal extent, and $0.5°$ in the meridional. Actually, we created two such data sets: one included all observations (day and night), and the other only observations during local nighttime hours to suppress the ionospheric component. The former data set was created to demonstrate that our data analysis approach does bring out field variations (of any origin, including ionospheric) with relatively short spatial scales, even if their magnitude is less than a few nT: as anticipated, one of the prominent features in Figure 9 is the Equatorial Electrojet (EEJ) which is observable only at daytime hours and is characterized by rather short spatial scales. Its position and width are in good agreement with previous, much more elaborate analyzes [e.g., *Lühr et al.*, 2004]. The absence of EEJ in the top panel of Figure 9 is due to the fact that zonal electric currents dominating EEJ induce only vertical and meridional components of the magnetic field. Furthermore, the binned data (with an average of about 10^2 measurements in each cell) were averaged within each cell followed by subtracting the 2.5-year mean for a given geographic location from the monthly means in each cell. The monthly fields were then smoothed using running averaging over 11 points in the meridional and 3 points in the zonal sections. These spatially smoothed residuals were ultimately used to compute standard deviations from the 2.5-year means.

[36] One important reason for using this quantity is that it must be strongly affected by magnetic field variations with timescales corresponding to quasi-geostrophic ocean currents. The deviations plotted in Figure 10 are free of ionospheric influences, although some effects of magnetosphere and/or lithosphere are apparent, for instance, as the North American anomaly. The zonal component is not shown in Figure 10 because, as pointed out earlier, EEJ
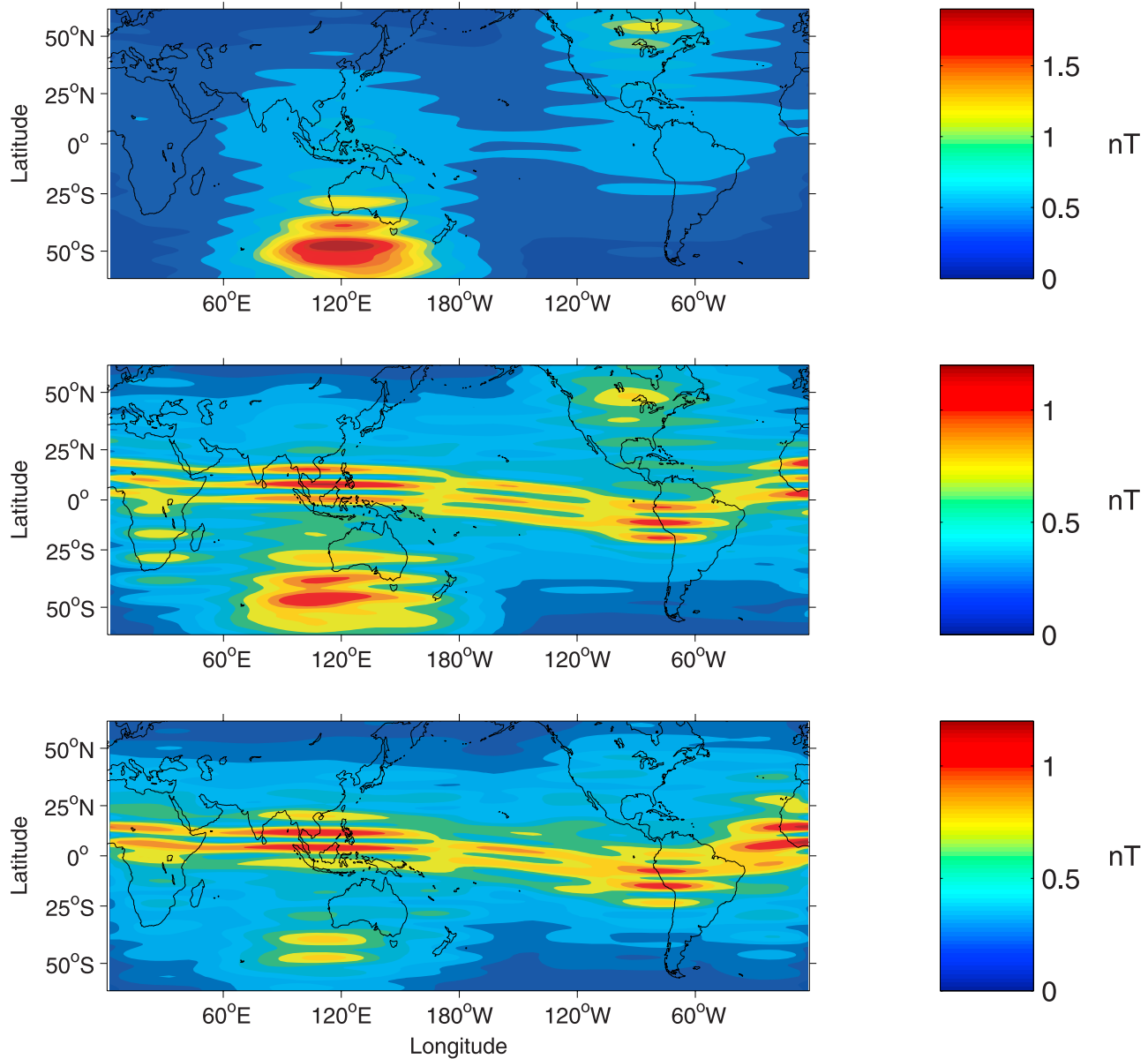
Figure 9. Standard deviation σ_b of the CHAMP-observed (bottom) vertical, (middle) meridional, and (top) zonal components of the residual field **b** from its 2.5-year mean.

does not induce this component; therefore, the removal of daytime measurements does not substantially affect the RMS deviation of b_x.

[37] The physical meaning of the quantity plotted in Figure 10 is closest to that shown in Figure 4 although the time interval corresponding to these RMS values is much shorter than the 11-year interval used for Figure 4. Comparing these results with the top panel of Figure 4, we conclude that the large variances in the region south of Australia are consistent with our model predictions both in terms of location and in terms of the magnitude of the field variance.

7. Analysis and Conclusions

[38] The very large (by comparison to the previous predictions) magnitude of the ocean-induced magnetic field at the sea surface is due to both a more accurate oceanographic model yielding significantly higher velocities of ocean currents and a more robust electro-magnetic model yielding a fully convergent solution for realistic input data. The predicted amplitude of field variations at the sea surface, on timescales from seasonal to inter-annual, makes the ocean-induced component to be a major factor of magnetic field variations to be observed by instruments situated at the sea surface and at aircraft altitudes. Such measurements, however, should be conducted over open ocean areas as opposed to island magnetometer observatories at which the second term in the r.h.s. of equation (10) vanishes and the first term dramatically decreases.

[39] The field magnitude predicted at the CHAMP altitude attains 6 nT. Given the 0.1 nT (or better) accuracy of the present satellite magnetometers, these values are within the reach of magnetometers flying at altitudes
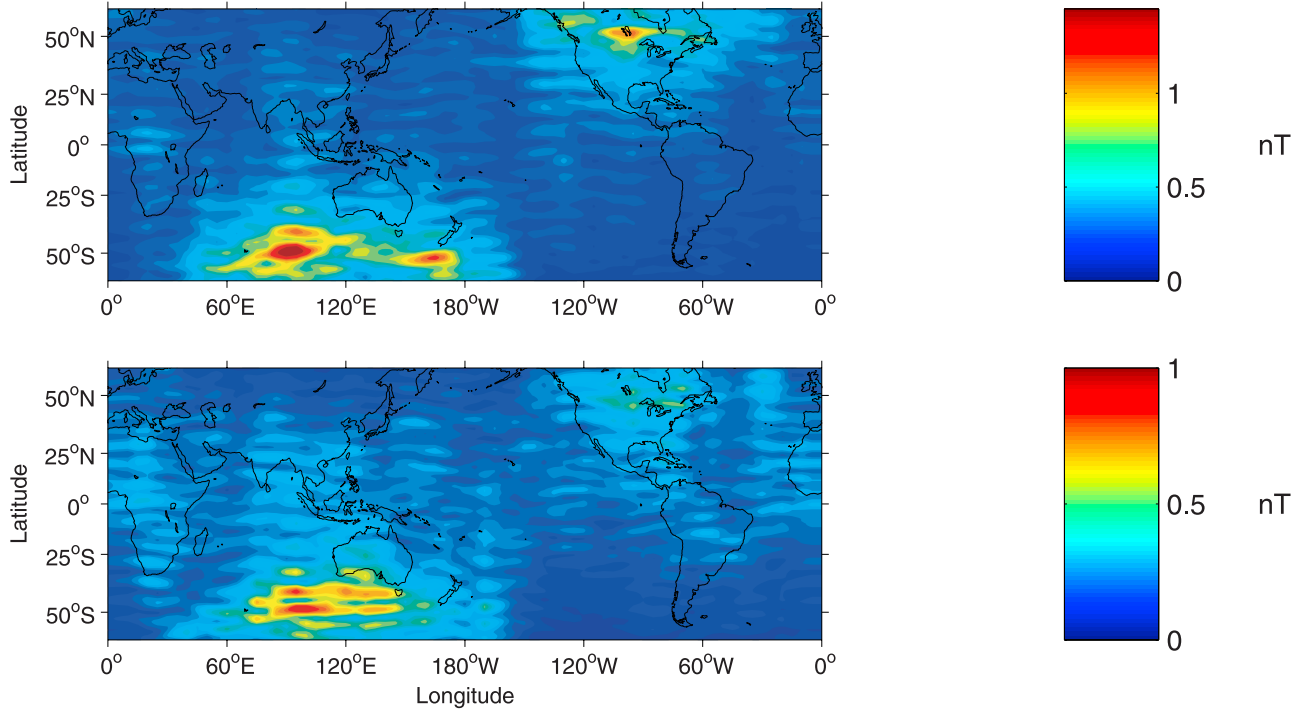
Figure 10. The same as Figure 9, but using only nighttime measurements to reduce ionospheric effects: standard deviation σ_b of the CHAMP-observed (bottom) vertical and (top) meridional components of the residual field **b** from its 2.5-year mean.

below 500 km. However, satellite measurements might, at best, detect only large scale variability associated with seasonal to inter-annual variability of horizontal oceanic transport averaged over large (about 500 km) sections. Ocean-induced fluctuations at annual and longer timescales are pronounced much stronger than higher-frequency fluctuations. Therefore such long-term oceanic variability may be more amenable to magnetometer-based detection than the higher-frequency components.

[40] Temporal fluctuations of the magnetic field about is long-term mean are rather small (see Figure 4). Their RMS value is in the $0.1-1.0$ nT range. Therefore their detectability in general is an open issue because it critically depends on the relative strength of non-oceanic fluctuations within selected ranges of spatial and timescales. However, in the area south of Australia, where these fluctuations attain their maximum, our preliminary analysis of the CHAMP satellite data appears to confirm the model predictions.

Appendix A

[41] The application of boundary condition (8) as well as a numerical solution of the Laplace equation for the magnetic field potential above the ocean surface is greatly facilitated by using a spherical harmonics decomposition. Relationships between the coefficients of expansion for the fields under consideration are provided by *Stephenson and Bryan* [1992] in their Appendix B. These relationships can also be used to elucidate the approximate condition (9).

[42] Neglecting the thickness, $H + h$, of the ocean-sediment system in comparison to the Earth's radius, a, the magnetic field potential beneath and above the "horizontal" boundaries of the shell is expanded as

$$\chi(\varphi, \theta, r)|_{r \leq a} = \sum_{n,m} \alpha_{nm} Y_{nm}(\varphi, \theta)(r/a)^n$$

$$\chi(\varphi, \theta, r)|_{r \geq a} = \sum_{n,m} \beta_{nm} Y_{nm}(\varphi, \theta)(r/a)^{-(n+1)}, \quad (A1)$$

where α_{nm} and β_{nm} are the expansion coefficients, and the radial coordinate, r, is related to z of section 2 as $z = r - a$. Substituting these expressions into equation (8) yields

$$\beta_{nm} = -\frac{n+1}{n}\alpha_{nm}. \quad (A2)$$

Note that if the ocean-induced variations of the field occur only on short (relative to the Earth radius) scales along the ocean surface, low-order terms in equation (A1) will have only a negligible contribution to the horizontal field $\mathbf{b}_\perp = \nabla_\perp \chi$. Really, the characteristic scale of $Y_{mn}(\varphi, \theta)$ variations decreases with an increasing n (because it is inversely proportional to the number of zeros of function Y_{nm}). It is easy to show that if the ocean-induced variations occur on scales shorter than, say, 600 km, the dominant contribution to $\mathbf{b}_\perp$ comes from the terms in equation (A1) with $n \geq 5$. However, for such large n, equation (A2) reduces to

$$\beta_{nm} \approx -\alpha_{nm}, \quad (A3)$$

which translates into the approximate boundary condition (9). For a planar shell, this condition is exact.

[43] Equation (14) presents the vertical jump, $\delta_z \mathbf{b}_\perp = \mathbf{b}_\perp(z = 0) - \mathbf{b}_\perp(z = -H - h)$, of the magnetic field as the surface gradient of a scalar function ψ. Expanding this function in spherical harmonics,

$$\psi(\varphi, \theta) = \sum_{n,m} \delta_{nm} Y_{nm}(\varphi, \theta), \tag{A4}$$

one can establish relationships (by means of equations (8) and (A2)) between the expansion coefficients,

$$\alpha_{nm} = \frac{n}{2n+1} \delta_{nm} \tag{A5}$$

$$\beta_{nm} = -\frac{n+1}{2n+1} \delta_{nm}. \tag{A6}$$

This facilitates the determination of magnetic potential χ at the shell boundaries based on $\delta_z \mathbf{b}_\perp$.

References

Chave, A. D., and D. S. Luther (1990), Low-frequency, motionally induced electromagnetic fields in the ocean, *J. Geophys. Res.*, *95*, 7185–7200.

Fletcher, C. A. J. (1988), *Computational Techniques for Fluid Dynamics*, vol. 2, 484 pp., Springer, New York.

Flosadottir, A. H., J. C. Larsen, and J. T. Smith (1997a), Motional induction in North Atlantic circulation models, *J. Geophys. Res.*, *102*, 10,353–10,372.

Flosadottir, A. H., J. C. Larsen, and J. T. Smith (1997b), The relation of seafloor voltages to ocean transports in North Atlantic circulation models: Model results and practical considerations for transport monitoring, *J. Phys. Oceanogr.*, *27*, 1547–1565.

Fukumori, I., R. Raghunath, L. Fu, and Y. Chao (1999), Assimilation of TOPEX/Poseidon data into a global ocean circulation model: How good are the results?, *J. Geophys. Res.*, *104*, 25,647–25,665.

Holme, R., N. Olsen, M. Rother, and H. Lühr (2003), CO2: A CHAMP magnetic field model, in *Proceedings of the First CHAMP Science Meeting*, edited by C. Reigber, H. Lühr, and P. Schwintzer, pp. 220–225, Springer, New York.

Jackson, J. D. (2002), *Classical Electrodynamics*, 3rd ed., John Wiley, Hoboken, N. J.

Kuvshinov, A., and N. Olsen (2004), 3-D modelling of the magnetic fields due to ocean tidal flow, in *CHAMP Mission Results II*, pp. 359–365, Springer, New York.

Larsen, J. (1992), Transport and heat flux of the Florida Current at 27°N derived from cross-stream voltages and profiling data: Theory and observations, *Philos. Trans. R. Soc. London, Ser. A*, *338*, 169–236.

Lee, J.-S. (1986), Speckle suppression and analysis for synthetic aperture radar images, *Opt. Eng.*, *25*(5), 636–643.

Lee, T., I. Fukumori, D. Menemenlis, Z. Xing, and L.-L. Fu (2002), Effects of the Indonesian Throughflow on the Pacific and Indian oceans, *J. Phys. Oceanogr.*, *32*, 1404–1429.

Lilley, F. E., J. H. Filloux, P. J. Mulhearn, and I. J. Ferguson (1993), Magnetic signals from an ocean eddy, *J. Geomagn. Geoelectr.*, *45*, 403–422.

Lilley, F. E., A. White, and G. S. Heinson (2001), Earth's magnetic field: Ocean contributions to vertical profiles in deep oceans, *Geophys. J. Int.*, *147*, 163–175.

Lühr, H., S. Maus, and M. Rother (2004), Noon-time equatorial electrojet: Its spatial features as determined by the CHAMP satellite, *J. Geophys. Res.*, *109*, A01306, doi:10.1029/2002JA009656.

Maus, S., and A. Kuvshinov (2004), Ocean tidal signals in observatory and satellite magnetic measurements, *Geophys. Res. Lett.*, *31*, L15313, doi:10.1029/2004GL020090.

Richtmyer, R. D., and K. W. Morton (1967), *Difference Methods for Initial-Value Problems*, 405 pp., Wiley-Intersci., Hoboken, N. J.

Sabaka, T. J., N. Olsen, and M. E. Purucker (2004), Extending comprehensive models of the Earth's magnetic field with Oersted and CHAMP data, *Geophys. J. Int.*, *159*, 521–547.

Sanford, T. B. (1971), Motionally-induced electric and magnetic fields in the sea, *J. Geophys. Res.*, *76*, 3476–3492.

Stephenson, D., and K. Bryan (1992), Large-scale electric and magnetic fields generated by the oceans, *J. Geophys. Res.*, *97*, 15,467–15,480.

Tyler, R. H., L. A. Mysak, and J. M. Oberhuber (1997), Electromagnetic fields generated by a three-dimensional global ocean circulation, *J. Geophys. Res.*, *102*, 5531–5551.

Tyler, R. H., S. Maus, and H. Lühr (2003), Satellite observations of magnetic fields due to ocean tidal flow, *Science*, *299*, 239–240.

Vivier, F., E. Maier-Reimer, and R. H. Tyler (2004), Simulations of magnetic fields generated by the Antarctic Circumpolar Current at satellite altitude: Can geomagnetic measurements be used to monitor the flow?, *Geophys. Res. Lett.*, *31*, L10306, doi:10.1029/2004GL019804.

_____

R. E. Glazman, Jet Propulsion Laboratory, M/S 300-323, 4800 Oak Grove Drive, Pasadena, CA 91109, USA. (reg@pacific.jpl.nasa.gov)

Y. N. Golubev, Raytheon ITSS, Pasadena, CA 91101, USA.